





Tomographic imaging of carbon dioxide in the exhaust plume of large commercial aero-engines

ABHISHEK UPADHYAY,¹  MICHAEL LENGDEN,^{1,*} GODWIN ENEMALI,² GEORGE STEWART,¹ WALTER JOHNSTONE,¹ DAVID WILSON,¹ GORDON HUMPHRIES,¹ THOMAS BENOY,¹ JOHN BLACK,¹ ANDREA CHIGHINE,² EDWARD FISHER,² RUI ZHANG,² CHANG LIU,² NICK POLYDORIDES,²  ALEX TSEKENIS,² PAUL WRIGHT,³ JOSHUA KLIMENT,³ JOHAN NILSSON,⁴  YUTONG FENG,⁴  VICTOR ARCHILLA,⁵ JAVIER RODRÍGUEZ-CARMONA,⁵ JESÚS SÁNCHEZ-VALDEPEÑAS,⁵ MARTA BELTRAN,⁶ VALENTIN POLO,⁶ IAN ARMSTRONG,⁷ IAIN MAUCHLINE,⁷ DOUGLAS WALSH,⁷ MARK JOHNSON,⁸ JOANNA BAULDREAY,⁹ AND HUGH MCCANN²

¹Department of Electronic and Electrical Engineering, University of Strathclyde, 204 George St., Glasgow, Scotland, UK

²School of Engineering, The King's Buildings, The University of Edinburgh, Edinburgh, UK

³Department of Electronics and Electrical Engineering, University of Manchester, Oxford Rd., Manchester, UK

⁴Optoelectronics Research Centre, University of Southampton, Highfield, Southampton, UK

⁵Instituto Nacional de Técnica Aeroespacial, INTA, Turbojet Engine Test Centre, Ctra. Ajalvir, km 4., Torrejón de Ardoz (Madrid), Madrid, Spain

⁶DAS Photonics, Ciudad Politécnica de la Innovación, Camino de Vera s/n. Acceso K, Edificio 8F, Valencia 46022, Spain

⁷Optosci Ltd., Netherthorpe, Langbank, Port Glasgow, PA14 6YG, UK

⁸Rolls-Royce, Test and Measurement Engineering, Derby, UK

⁹Bauldreay Jet Fuel Consulting Ltd., 14 Grosvenor Court, Foregate Street, Chester, Cheshire, CH1 1HG, UK

*Corresponding author: michael.lengden@strath.ac.uk

Received 1 July 2022; revised 1 September 2022; accepted 4 September 2022; posted 6 September 2022; published 29 September 2022

We report here the first implementation of chemically specific imaging in the exhaust plume of a gas turbine typical of those used for propulsion in commercial aircraft. The method used is chemical species tomography (CST) and the target species is CO₂, absorbing in the near-infrared at 1999.4 nm. A total of 126 beams propagate transverse to the plume axis, along 7 m paths in a coplanar geometry, to probe a central region of diameter ≈ 1.5 m. The CO₂ absorption spectrum is measured using tunable diode laser spectroscopy with wavelength modulation, using the second harmonic to first harmonic (2f/1f) ratio method. The engine is operated over the full range of thrust, while data are recorded in a quasi-simultaneous mode at frame rates of 1.25 and 0.3125 Hz. Various data inversion methodologies are considered and presented for image reconstruction. At all thrust levels a persistent ring structure of high CO₂ concentration is observed in the central region of the measurement plane, with a raised region in the middle of the plume assumed to be due to the engine's boat tail. With its potential to target various exhaust species, the CST method outlined here offers a new approach to turbine combustion research, turbine engine development, and aviation fuel research and development.

Published by Optica Publishing Group under the terms of the [Creative Commons Attribution 4.0 License](https://creativecommons.org/licenses/by/4.0/). Further distribution of this work must maintain attribution to the author(s) and the published article's title, journal citation, and DOI.

<https://doi.org/10.1364/AO.467828>

1. INTRODUCTION

Aviation is a significant and growing contributor to global emissions of carbon dioxide (CO₂), and both short-haul and long-haul air travel are projected to increase in future decades [1–4]. The aviation industry in the EU has therefore pledged to achieve at least 75% CO₂ and 90% NO_x reductions by 2050 [4]. A number of strategies are under consideration to curb air travel emissions, including but not limited to continued improvements in the efficiency of turbine engines, use

of sustainable aviation fuels (SAFs), and electrically driven propulsion. The first two of these options require improved monitoring and/or deeper understanding of turbine combustion, while the third is limited for aerospace applications due to the required energy densities, particularly for medium and large civil aircraft, favoring the continued use of liquid fuel and limiting the application of electrical technology. Therefore, the pressing requirement to further improve efficiencies in

large-scale liquid-fuelled aero-engines drives a need for effective measurement strategies of their combustion behavior, e.g., to provide a better understanding of emissions generation processes and improved knowledge of the influence of fuel compositions.

The current practice for the quantification of gaseous emissions from large-scale commercial aero-engines is the use of gas chromatography, where samples are obtained using extractive sampling from the exhaust. This technique is highly intrusive, affecting the performance of the engine in an unknown manner. In some cases, the extraction probe can be moved spatially in one or two axes, providing limited spatial resolution of the exhaust. However, the temporal resolution is poor, as the measurement equipment is typically located outside the building used to test the engine, and there is a measurement lag as gases flow through the sampling pipe. Furthermore, continued chemical reactions within the extraction pipework result in significant measurement uncertainties. The ability to measure gaseous species in an *in situ*, noninvasive manner with improved spatial and temporal resolution will therefore improve the validity of emissions measurements as well as reducing the overall time and cost required for testing.

Chemical species tomography (CST) uses optical absorption to achieve imaging of the spatial distribution of gaseous species [5] in a manner analogous to x-ray computed tomography. Therefore, CST can be implemented by extending single-channel tunable diode laser spectroscopy (TDLS) using multiple beam paths to extract 2D spatial information of the concentration distribution of a target species [5–7]. TDLS is advantageous for aero-engine applications, as it is a noninvasive, *in situ* technique that has a number of proven methodologies for harsh environments. This has led to TDLS-based CST being demonstrated in various industrial process applications [8–11], with an emphasis on combustion-related cases. For example, in the compression-ignition automotive engine case [9], 31 beams imaged diesel fuel distribution within the 81 mm diameter cylinder at 3000 frames per second (fps) with typical spatial resolution of 9 mm [12].

In this paper we present results from a consortium of university research teams and industrial partners on the development of a large-scale CST imaging system to measure the cross-sectional distribution of CO₂ in the exhaust of commercial aero-engines [13–17]. The specific TDLS approach used is wavelength-modulation spectroscopy (TDLS-WM), which is often classified as being calibration-free due to its ability to normalize for optical intensity directly from the optical signal that also measures the gas-dependent optical absorption [18,19]. In TDLS-WM, the laser diode is simultaneously current driven by a low-frequency sawtooth or sinusoidal current ramp (typically 5–50 Hz) and a high-frequency sinusoidal current modulation (typically 10–100 kHz). The low-frequency waveform is used to wavelength-tune over an absorption line of interest, while the high-frequency current modulation results in high-frequency wavelength modulation (WM) and intensity modulation (IM) outputs from the laser. The interaction of the WM and IM signals with the target gas species generates a number of gas-dependent optical signals at the harmonics of the modulation frequency, which can be measured using lock-in amplification. However, in TDLS-WM there are also harmonic signals



Fig. 1. Optical mounting frame (red) behind a large scale commercial aero-engine at the engine test bed facility at Instituto Nacional de Técnica Aeroespacial (INTA), Madrid.

generated by the direct IM from the laser, defined as the linear (first harmonic) and nonlinear (second and higher harmonics) residual amplitude modulation (RAM) terms. A number of TDLS-WM methodologies have exploited this RAM term as a normalization constant, removing any intensity dependence on recovered gas signals [18–25]. These techniques therefore have the capability of removing the significant optical noise generated by beam steering effects in the exhaust plume and mechanical vibration of the optical mounting in the engine test bed.

The exhaust imaging space required for large-scale commercial engines can be up to 1.8 m diameter, and in this work all optical components were mounted on a 7 m diameter frame (Fig. 1) located 3 m downstream of the exit nozzle of the engine. To achieve a target spatial resolution of ≈ 60 mm in the central region [26] and to allow for potential malfunctions in the hostile environment of the engine test cell, 126 optical beams are used in six angular projections that each contain 21 parallel beams (as shown in Fig. 5). Therefore, an optical source is required with high power and the ability for optical distribution. As the optical power output from semiconductor laser diodes that provide suitable current and wavelength tunability is typically <10 mW, a maximum optical power of no more than 80 μ W will be available per beam. The use of optical fiber amplifiers in a master oscillator power amplifier (MOPA) configuration allows the diode power to be amplified to the watt scale, while maintaining the relevant modulation characteristics of the seed diode source and constraining the light within optical fiber [27]. This technique also allows the distribution of light around the ring using a fiber splitter network.

The development processes of the optical measurement techniques [14,17], optomechanics, mechanical structure [15], and measurements using a controlled phantom [16,28] have been described previously. In this paper, we present the current measurement status beginning with an introduction to the spectral selection for CO₂ measurements. A brief description

is then given of the image reconstruction process and the two algorithms that have been used, viz. Tikhonov regularization [7] and the Landweber method [29–31]. The experimental methodology is described, including a quasi-parallel data-acquisition system based on a National Instruments (NI) PXI chassis and an analysis of the system performance. The measurements using a controlled phantom are then revisited by considering the effect of optical beams lost prior to engine measurement. Finally, aero-engine exhaust images are presented for different high-pressure-compressor-shaft-speed (NH) levels from 62.5% to 96.3% at frame rates of 1.25 Hz and 0.3125 Hz.

2. SPECTRAL ANALYSIS

Optical amplification using a MOPA is possible at the CO₂ absorption regions located at 1550 nm and 2000 nm, using either an erbium-doped fiber amplifier or a thulium-doped fiber amplifier (TDFA), respectively. The higher achievable sensitivity at 2000 nm makes it the preferred option, even though optical detection and fiber delivery is more complex. The assumed conditions during engine operation were 3% CO₂ and 5% H₂O at 600°C in plume and 400 ppm CO₂ and 3% H₂O at 20°C out of plume. Each beam path is 7 m in length, and the assumed plume diameter is ≈ 1.4 m. In previous work, the HITRAN2008 database [32] was used to identify the R(48)_e CO₂ transition at 1997.2 nm as being free from major interference from water vapor. However, during a measurement campaign at the Gas Turbine Research Centre, Cardiff, where CO₂ was measured in the exhaust of a combustor at temperatures above 600°C [33], interfering spectral features were identified. Figure 2 shows spectral data for CO₂ and H₂O at a central wavelength of 1997.2 nm. The modeled high-temperature H₂O spectrum using parameters from the HITEMP2010 database is shown in gray, while the broken cyan line shows the modeled high-temperature spectrum for H₂O using parameters from the HITRAN2008 database. A number of spectral features of water vapor are present in HITEMP2010 that are not present in the HITRAN2008 model used to identify a suitable absorption feature in 2010. These new spectral features are present in both the HITEMP database [34] and versions of the HITRAN database from 2012 [35]. These new water vapor features cause significant distortion to the

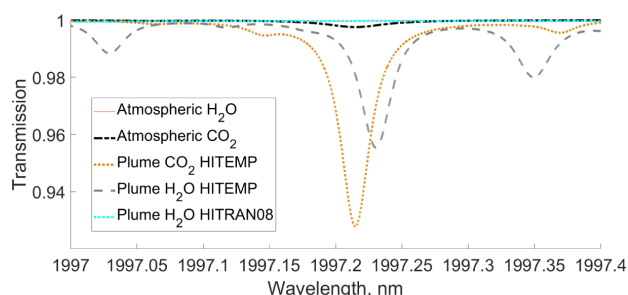


Fig. 2. Spectral data for CO₂ and H₂O at a central wavelength of 1997.2 nm. The high-temperature H₂O spectrum using HITEMP2010 database (broken gray line) is significantly different from the high-temperature H₂O spectrum using HITRAN2008 (broken cyan line). The high-temperature CO₂ (broken orange), atmospheric CO₂ (broken black), and atmospheric H₂O (red) are plotted using the HITEMP2010 database.

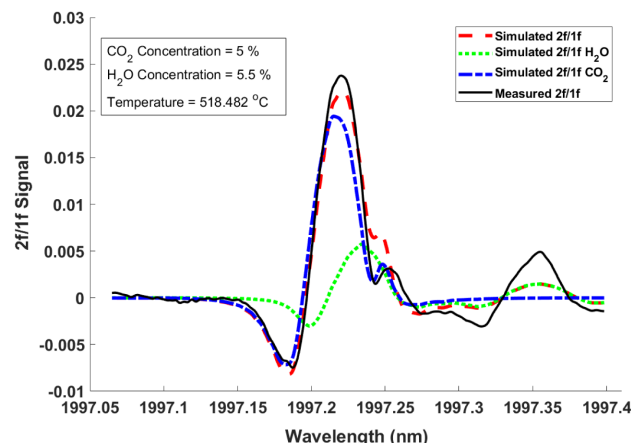


Fig. 3. Recovered spectral data of CO₂ and H₂O within the exhaust of a combustor at the University of Cardiff, and a comparison with a theoretical fit for both species. It is evident that one H₂O feature is causing significant interference in the recovered CO₂ feature. Also, there is a clear mismatch with the experimentally recovered data and the fitting of the water vapor features.

CO₂ signal, and as discussed below they still do not match the experimental spectra.

Figure 3 shows the experimental signal (solid black) recovered from the exhaust at Cardiff, and a comparison with a theoretical fit for both species. The 2010 version of the HITEMP database was used to model the H₂O and CO₂ spectral features. The temperature inferred by fitting a simulated 2f/1f signal (broken red) to the experimental signal was 518°C, and the concentrations inferred for CO₂ and H₂O were 5% and 5.5%, respectively. The corresponding signals for CO₂ and H₂O are shown by broken green and broken blue lines, respectively. For any combination of temperature and concentration values of the two gases, it was not possible to simultaneously obtain a good fitting for the two regions near 1997.24 nm and 1997.36 nm. Therefore, there is still significant doubt that the model is providing accurate spectral parameters for these particular water vapor and carbon dioxide features.

Another CO₂ line at 1999.4 nm has been identified, which is still shown to be free from interference in both the HITRAN2012 and HITEMP2010 databases, as shown in Fig. 4. All data presented in this present paper targets this new CO₂ feature using a distributed feedback interband cascade laser centered around 1999.4 nm (Eblana Photonics). It must be noted that this spectral region does show a larger degree of distortion due to background CO₂, which has to be considered during the measurement process. This can be achieved by measuring the background CO₂ using one of the optical beams located at the edge of the imaging plane that does not intersect with the plume, or alternatively measuring the background CO₂ concentration before starting the engine and subtracting this value from the calculated path concentration integrals obtained during the test; we have used the latter approach for the results presented in this paper. In the next section, we describe a methodology to isolate the issue of disentangling the effects of concentration and temperature to derive the required estimates of path concentration integral, along each beam, from the measured spectral data.

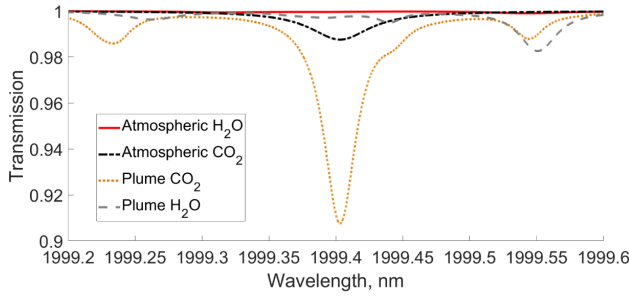


Fig. 4. Spectral data for CO₂ and H₂O at a central wavelength of 1999.4 nm. There is less distortion caused by H₂O at this wavelength. However, careful consideration needs to be given to the background CO₂ levels, which cause a higher overall contribution as compared to 1997.2 nm.

3. ABSORPTION TOMOGRAPHY

In classical absorption tomography, simultaneous multiple line of sight (LOS) integrated absorption measurements obtained from different angular projections are used to obtain an image of the attenuating material through which the beams propagate. Estimation of the distribution of the attenuating material from the inevitably imperfect absorption measurements is inherently ill-posed, e.g., see [36]. In CST, the spatial constraints, cost of implementation and the achievable optical power imply that the number of beams is typically much lower than the desired number of pixels in the reconstructed image, resulting in a so-called discrete ill-posed problem [5,37] in which the underlying system of equations is also rank deficient. Hence, regularization techniques are often used that assume some degree of *a priori* information, such as non-negativity constraint or smoothness of the flow field [5,16,37]. In this paper, we have used two regularization techniques that have proven effective for such rank deficient problems, Tikhonov regularization [37,38] and the Landweber method [29–31]. Tikhonov regularization is noniterative and is typically less computationally intensive, whereas the Landweber method is an iterative approach that can provide improved imaging accuracy but at the cost of computation time. A brief description of the mathematical formulation for both these approaches is provided in this section. In the 2f/1f method [18–25], the experimental signal obtained by taking the ratio of the first harmonic (2f) and the fundamental (1f) signals is fitted to the corresponding simulated signal to obtain the gas parameters. Traditionally, ratio thermometry that uses two significantly different spectral transitions is used to obtain the average temperature of the target gas interacting with the beam. Once this temperature is obtained, then either line can be used to obtain the average concentration of the target gas [19,23,25,39–42]. However, as shown in [33], a single spectral transition can also be used to obtain average concentration and temperature simultaneously using nonlinear fitting, provided the line-strength value is monotonically increasing or decreasing in the desired temperature range. For the selected 1999.4 nm line, over the temperature range used during this test (i.e., 400–700°C) there are no multiple temperature values with equal values of line strength, therefore allowing direct fitting for average concentration and temperature values. Therefore, in this paper, the latter technique has been used to obtain the integral of CO₂ concentration along each of the 126 beam paths. Since the

gas temperature is a nonlinear function of the absorption signal and hence of the 2f/1f signal, linear tomography cannot be used to obtain its spatial distribution. However, variation of concentration with absorption signal is almost linear, and therefore linear tomography methods can be applied to obtain the spatial distribution of the concentration using the path concentration integrals retrieved using the 2f/1f method for each beam.

Our system consists of k ($= 126$) beams passing through the region of interest (ROI) that is divided into n ($= 80 \times 80$) pixels. Each independent LOS measurement of the average concentration for the r^{th} beam, b_r , recovered by the method described in the above paragraph, can be described as follows:

$$b_r = \frac{1}{L} \int_L x dl = \frac{1}{L} \sum_{j=1}^n l_{r,j} x_j, \quad (1)$$

where x_j is the concentration within the j^{th} pixel (assumed uniform), $l_{r,j}$ is the intersection length of the r^{th} beam with the j^{th} pixel, and L is the distance between source and detector, which was 7 m for all 126 beams. Equation (1) can also be represented in matrix form as follows:

$$\mathbf{b} = \mathbf{A}\mathbf{x}, \quad \text{where } \mathbf{b} = \hat{\mathbf{b}} + \delta\mathbf{b}. \quad (2)$$

Here, $\mathbf{x} = [x_1, x_2, x_3, \dots, x_n]^T$ is the vector of gas concentrations in n pixels (i.e., the desired image), $\mathbf{b} = [b_1, b_2, b_3, \dots, b_k]$ is the vector of fitted average concentrations of all 126 beams, with $\hat{\mathbf{b}}$ and $\delta\mathbf{b}$ as its noise free and additive noise components. A detailed analysis of the noise in the measurement data for the engine test results is provided in Section 7. \mathbf{A} is the weighting coefficient matrix, arising from the discretization of the integral in Eq. (1), for n pixels and k beams, $\mathbf{A} \in \mathbb{R}^{k \times n}$.

$$\mathbf{A} = \begin{pmatrix} l_{1,1} & l_{1,2} & \dots & l_{1,n} \\ \vdots & \vdots & \vdots & \vdots \\ l_{k,1} & l_{k,2} & \dots & l_{k,n} \end{pmatrix}. \quad (3)$$

In Tikhonov regularization, the rank-deficient system described by Eq. (2) is augmented with extra rows that also enforce a smoothness criterion. The regularized solution is the vector \mathbf{x}_λ that minimizes the residual norm of the augmented matrix for the given regularization parameter λ and is given by

$$\mathbf{x}_\lambda = \text{argmin}\{\|\mathbf{A}\mathbf{x} - \mathbf{b}\|_2^2 + \lambda^2 \|\mathbf{M}\mathbf{x}\|_2^2\}, \quad (4)$$

where $\mathbf{M} \in \mathbb{R}^{n \times n}$ is a Laplacian matrix used to enforce smoothness in the profile of the concentration images, and its elements are given by

$$\mathbf{M}_{(u,v)} = \begin{cases} 1 & u = v \\ \frac{-1}{\text{number of neighbours}} & u \text{ neighbours } v \\ 0 & \text{otherwise,} \end{cases} \quad (5)$$

where pixel u is neighbor to pixel v if they share at least one vertex. The regularization parameter λ can be determined by the L-curve method [43] or by a method based on singular value decomposition (SVD) of the augmented matrix [37]. In this paper, we have used the L-curve method. The L-curve is obtained by plotting the two norms of the Tikhonov objective function, $\|\mathbf{A}\mathbf{x} - \mathbf{b}\|_2^2$ and $\|\mathbf{M}\mathbf{x}\|_2^2$, given by Eq. (4), often

referred to as “residual norm” and “regularization norm,” respectively. A solution on the vertical part of the L-curve is dominated by the residuals, i.e., by the measurement errors. Similarly a solution on the horizontal part of the L-curve is dominated by smoothness, i.e., by the regularization errors. Therefore, a good trade-off is obtained at the corner of the L-curve, and the corresponding λ value would provide the optimal solution.

The second method used in this paper is the modified Landweber method, which is an iterative approach [29]. In the Landweber method, the unknown concentration vector \mathbf{x} is updated from iteration t as

$$\mathbf{x}^{t+1} = \mathbf{x}^t + \alpha \mathbf{A}^T (\mathbf{b} - \mathbf{A}\mathbf{x}^t), \quad (6)$$

where t is the index for the current iteration, and α is the relaxation parameter that is constant for all iterations for our work. The Landweber method tries to minimize the image approximation error and solves the following problem:

$$\mathbf{x} = \operatorname{argmin}\{\|\mathbf{A}\mathbf{x} - \mathbf{b}\|^2\}. \quad (7)$$

In the absence of any filtering, like most iterative approaches, Landweber is also semi-convergent, and a stopping criterion must be used to obtain the minimum norm solution; further iterations would typically lead to an increase in total error. However, since the reconstructed gas distribution is expected to be continuous, we can introduce the prior information of local smoothness using a median or a mean filter. In this work, after each iteration, the image was filtered with a median filter of dimension 5×5 . This application of the filter, along with introducing smoothness in the reconstructed images, removes the semi-convergence nature of the Landweber method as the iterations converge to a single solution [30,31]. Therefore, in this paper the iterations were stopped when the change in the residual norm was less than 10^{-3} , i.e., $\|\mathbf{A}\mathbf{x}^{t+1} - \mathbf{b}\|^2 - \|\mathbf{A}\mathbf{x}^t - \mathbf{b}\|^2 < 10^{-3}$. The relaxation parameter α_t was taken as constant for all iterations, and its

optimum value was chosen using the dual burner phantom test described in Section 6.

4. EXPERIMENTAL SETUP

The experimental setup is shown in Fig. 5. The laser module is a SMF-28 fiber coupled interband cascade laser (ICL), housed within a commercial current and temperature control unit, with remote operation capabilities using either USB or ethernet (Optosci Ltd). The output from the laser passes through a 1×2 optical fiber coupler, with one output connected to a Mach-Zehnder interferometer and the other output connected to a commercial TDFA from Lumibird. The TDFA has a maximum output of 1 W and contains an internal 1×6 output coupler resulting in a total output of 167 mW per channel. The light from each of the six TDFA output channels is transmitted into the aero-engine test bed using 40 m SMF-28 Kevlar fiber patch cables. Each patch cable is connected to one of six bespoke 1×21 fiber splitter units (Gooch and Housego) located on the odd vertices of the dodecagonal 7 m diameter mounting frame [13]. Each output from the 1×21 couplers is transmitted by an SM2000 fiber patch to a bespoke optical launch unit, which consists of an angled FC-APC fiber puck and a plano-convex spherical lens of 75 mm focal length and 25.4 mm diameter [15]. The maximum power that can be launched from each optical launch unit is therefore 8 mW, assuming no losses around the distribution network. The light from the launch unit is transmitted across the frame onto a bespoke receiver unit, which contains a second 75 mm focal length lens that focuses light onto a 1 mm^2 extended InGaAs photodiode. Each optical signal is converted into a differential voltage signal using a bespoke pre-amplifier that incorporates a line driver [13], affording some immunity to ambient noise in the engine test cell. For the data presented in this paper, twelve 60 m lengths of unshielded ribbon cable were used to provide electrical power to the photoreceivers and pre-amplifiers, and to carry the 126

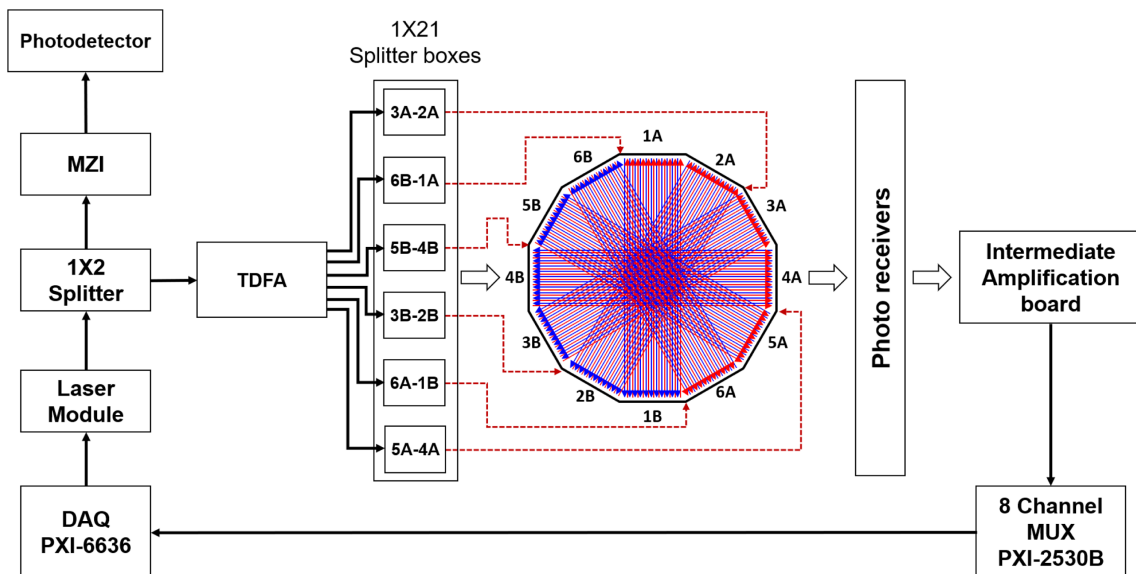


Fig. 5. Experimental setup. All equipment is located outside the engine test bed except for the 1×21 splitter units, optical ring, and the 126 photoreceivers.

differential output signals out of the engine test cell. Each differential signal was then converted to single-ended, at unity gain, using a bespoke intermediate amplification board (IAB) that also presented the output signals in groups of eight to the DAQ system described below.

A NI PXI chassis system is used for laser current modulation control and data acquisition, all of which is operated using LabVIEW. Two analogue outputs from a NI PXIe-6366 data acquisition board are used to provide either a 5 Hz or 20 Hz sawtooth waveform combined with a 100 kHz sinusoidal waveform to the Optosci current driver unit. The PXIe-6366 board has eight analogue inputs, each with 16-bit vertical resolution and a $2 \text{ MSs}^{-1} \text{ channel}^{-1}$ sampling rate. A NI PXI-2530B multiplexer unit is used to measure all 126 channels, sequentially in groups of eight, as output from the IAB, resulting in a full acquisition of a frame in 16 steps, i.e., the frame rate of acquisition is $20/16 = 1.25 \text{ Hz}$. The PXI also contains a NI PXIe-4113 programmable power supply, with a maximum output of 6 A, which is used to power all 126 photoreceiver pre-amplifiers and the IAB. Finally, the PXI chassis, which contains an *i7* processor, is used to buffer the collected data onto a 1 TB solid-state hard drive for analysis. Once the full engine test has run, all the obtained WMS signals are demodulated using a software lock-in amplifier (LIA) code written in LabVIEW. Simultaneously, all laser wavelength modulation characteristics are measured using the Mach-Zehnder interferometer to allow full laser characterization for modeling the obtained spectral signals [44].

5. SYSTEM PERFORMANCE

The entire ring structure, including all optical and electronic components, was constructed outside the aero-engine test bed when the frame was in a horizontal position. The frame was then transferred into the test bed using the same crane and pulley system that is used to transfer an aero-engine. During the transfer process, a number of the optical components were either damaged or misaligned and were therefore non-operational for these initial measurements. The non-functioning beams are highlighted in red in Fig. 6.

The $2f/1f$ technique requires the laser's characteristics to be included within the TDLS-WM model [19]. Specifically, the method requires ratios of the DC laser intensity, I to the linear (ΔI) and nonlinear (ΔI_2) intensity modulation (IM) amplitudes, the wavelength modulation amplitude (WM) amplitude $\delta\lambda$, and the phase between the WM and IM signals, at the fundamental frequency and the second harmonic ϕ and ϕ_2 , respectively.

The first major consideration regarding sensor performance is the translation of the WM and IM characteristics of the ICL seed laser during the TDFA amplification process. Figure 7 shows the DC intensity and the linear intensity modulation output from both the laser and the TDFA and the generated $I/\Delta I$ for each case. The TDFA is clearly operating in gain saturation, as the laser intensity output flattens out significantly. However, the gain saturation affects the IM amplitude output from the TDFA to the same degree, resulting in minimal variation in the $I/\Delta I$ output from the TDFA as compared to the direct laser output. As the TDFA has no effect on the wavelength of the light being amplified, there is also no variation in the WM amplitude.

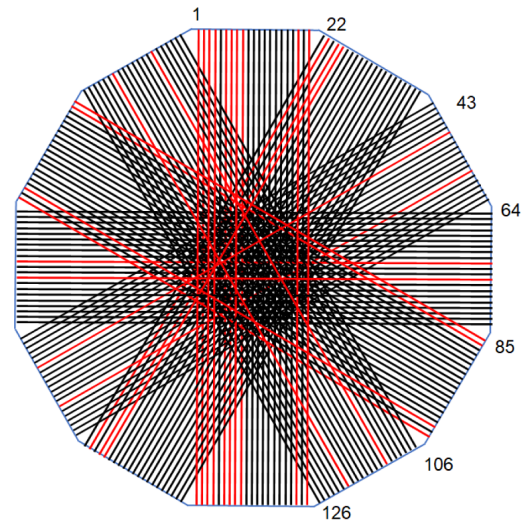


Fig. 6. Location of all 126 beams on the 7 m frame, showing the concentration or density of beam intersections in the ROI. Beams that were non-operational during these tests are shown in red.

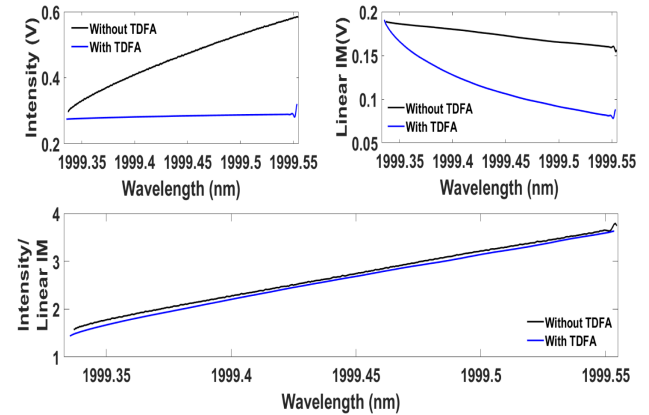


Fig. 7. Characterization of the direct laser output and the output after the TDFA that shows gain saturation. However, the $I/\Delta I$ output from both devices show very little variation.

Therefore, all laser characteristics can be measured using the TDFA setup in the same manner as for a single laser diode.

During a measurement campaign the values for $I/\Delta I$, $I/\Delta I_2$, ϕ , and ϕ_2 are measured individually for each of the 126 channels as follows: initially, the photodiode dark current is recorded for each channel using the PXI DAQ system; the laser and TDFA are then switched on and left to stabilize for 30 min, and the intensity modulated output of each individual channel is recorded. The DC intensity for each channel, I , is obtained by passing the intensity modulated signal through a digital low-pass filter and then subtracting the dark current signal. ΔI and ϕ are measured for each channel by passing the intensity modulated signals through the digital LIA. Here ΔI is obtained by taking the magnitude of the $1f$ output of the LIA, and ϕ is obtained by aligning the phase of the LIA along the $1f$ -WM component and then using the following ratio to obtain the phase

$$\frac{Y_{nf}^{\text{nogas}}}{X_{nf}^{\text{nogas}}} = \frac{\Delta I_n \sin(\phi)}{\Delta I_n \cos(\phi)} = \tan(\phi), \quad (8)$$

where X_{nf} and Y_{nf} are the in-phase and quadrature outputs of the LIA for the n th harmonic. A more detailed description of the methodology to obtain these parameters can be found at [33,45].

6. IMAGE RECONSTRUCTION AND VALIDATION

Prior to the transfer of the ring into the test bed, a full system check was carried out using measurements of CO_2 produced by gas burners placed at different locations in the ROI as described previously [16,28] and as shown in Fig. 8.

During this validation campaign the ring was lying horizontally, and the exit plane of the burners was located just below the level of the transmit/receive plane. In these tests, all 126 beams yielded robust signals. For all image reconstructions presented in this paper, the ROI is defined to be the central square of side



Fig. 8. Dual burner test with the ring lying horizontal.

length 165 cm within the measurement plane, and it is discretized into $n = 80 \times 80$ pixels, resulting in a pixel size of about 2 cm.

Figure 9 shows the case where two gas burners of diameter 40 and 60 cm are placed within the ROI with their edges 20 cm apart. Each subfigure of Fig. 9 shows two circles inscribed in a larger circle. The outer circle of 140 cm diameter was drawn at the test site, when the ring was lying horizontally, with its center being concentric with the center of the ring. The two inner circles represent the location of the two burners (diameters 40 and 60 cm) that were placed inside the outer circle with their edges being tangential to the outer circle. The NI PXI-2530B multiplexer unit was not available for these tests, and therefore data from eight channels were obtained sequentially. The rest of the experimental setup was the same as described in Section 4, with the laser operating with a 5 Hz ramp. In previous publications, we presented images for this setup using a constrained solver for all 126 beams [16,28]. In this paper, we have considered the use of both Tikhonov regularization and the Landweber method, and we have assessed the effect of removing all beams that were not operational during the engine test measurement campaign, highlighted in Fig. 6.

Figure 9(a) shows the reconstructed image using first-order Tikhonov regularization with smoothness constraint using all the 126 beams, while (b) shows the reconstructed image with the removal of the non-operating beams. Similarly, Figs. 9(e) and 9(f) show the images recovered using Landweber for 126 beams and with the non-operating beams removed, respectively. The L-curve plot described in Section 3 is shown in Fig. 10 and λ values at the corner range from 10 to 100. Hence, the images shown in Fig. 9 are generated with $\lambda = 50$.

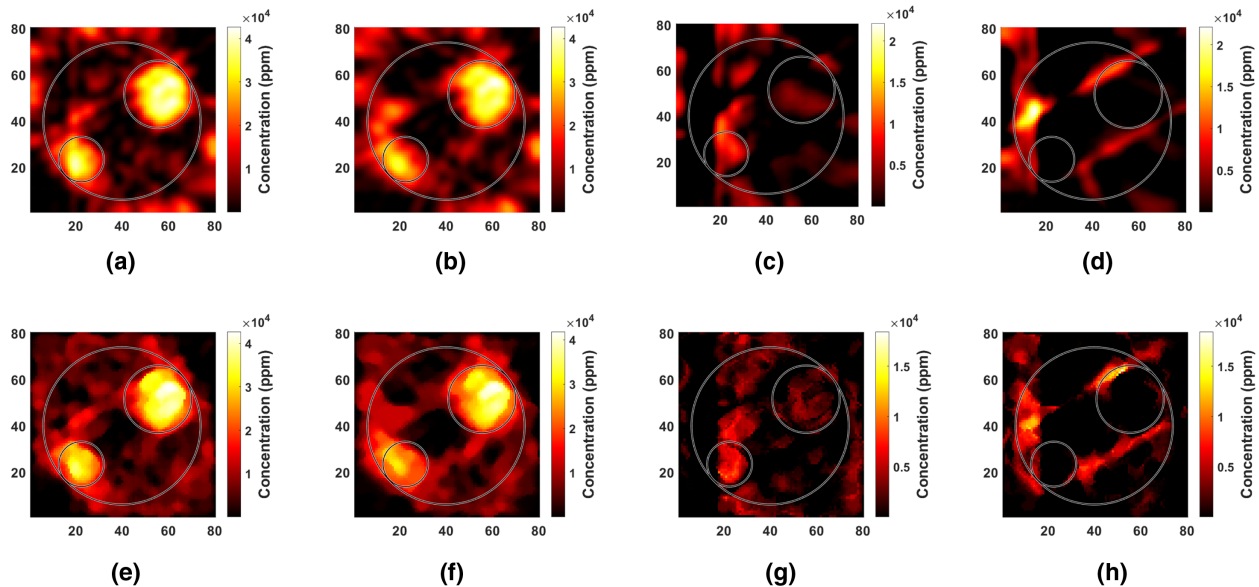


Fig. 9. Concentration distribution recovered in the ROI using Tikhonov regularization and the Landweber method, before and after excluding the dead beams. Each panel above shows the reconstructed 80×80 pixel image in the ROI, which is the central square of side length 165 cm in the measurement plane. (a) Tikhonov with all beams. (b) Tikhonov with non-operational beams removed. (c) Difference Tikhonov (with all beams–non-operational beams removed). (d) Difference Tikhonov (non-operational beams removed–with all beams). (e) Landweber with all beams. (f) Landweber with non-operational beams removed. (g) Difference Landweber (with all beams–non-operational beams removed). (h) Difference Landweber (non-operational beams removed–with all beams).

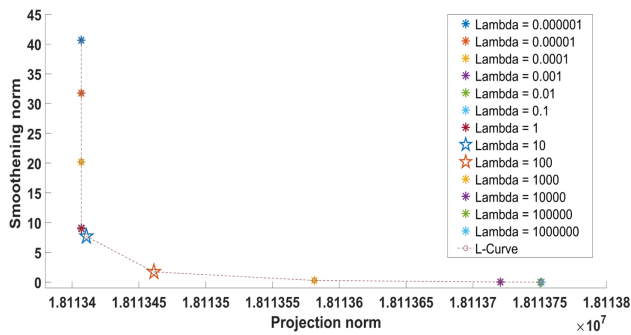


Fig. 10. L-curve plotted using regularization parameters ranging from 10^{-6} to 10^6 . The most suitable value where neither the smoothing norm nor the residual norm is dominating the solution is obtained at the corner of the L-curve, i.e., for values between 10 and 100.

For the Landweber algorithm it is known that the relaxation parameter α_t must be less than $(2/\max(\text{eigs}(\mathbf{A}^T\mathbf{A}))$ for convergence [46]. It is also known that the larger step size would result in faster convergence, but there is no closed-form method for obtaining parameters α_t . However, since we already know the burner locations, and we also know that the imaging plane is just above the burners; therefore, the regions of maximum concentration would be just above the burner locations. Using this *a priori* information along with others such as smoothness, the relaxation parameter obtained for the Landweber algorithm was $\alpha = 0.0046$. The reconstructed images using these parameters are shown in Figs. 9(e) and 9(f). The same parameters were used for reconstruction of the images for the engine test measurements discussed in Section 7. As discussed in Section 3, the iterations in the Landweber method were stopped when the change in residual norm was less than 10^{-3} . Therefore, using this stopping criterion and with $\alpha = 0.0046$ as the relaxation parameter, the number of iterations required to reconstruct the images shown in Figs. 9(e) and 9(f) were 25 and 46, respectively.

In Fig. 9(c) the image reconstructed with the non-operational beams removed was subtracted from the image reconstructed with all the 126 beams, using the Tikhonov method. In Fig. 9(d) the subtraction was done in the reverse order. Figures 9(g) and 9(h) show the results of both these subtractions for the Landweber method. The negative values in Figs. 9(c), 9(d), 9(g), and 9(h) were taken as zeros. It can be observed that for both Tikhonov and Landweber methods the removal of the non-operational beams from the image reconstruction resulted in a lower prediction of the CO_2 at the burner locations, i.e., some of the CO_2 that would have been predicted within the burner locations when all the beams were operational, was predicted outside the burner location due to the removal of non-operational beams, as shown in Figs. 9(c), 9(d), 9(g), and 9(h). Therefore, we can expect a similar effect for the engine test measurements as well.

7. RECONSTRUCTED IMAGES DURING ENGINE TESTING

A full CO_2 imaging campaign was carried out for a Trent engine operating at four different thrust conditions corresponding to NH values of about 61.2%, 72.05%, 82.63%, and 96.28%.

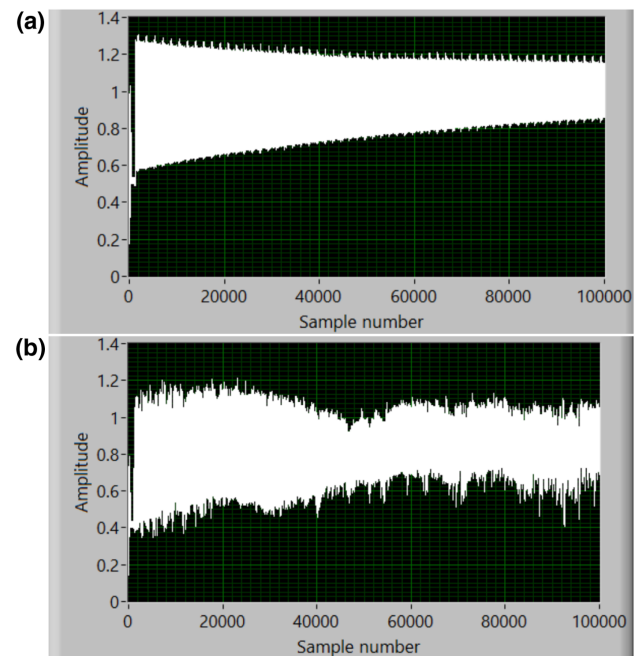


Fig. 11. Raw output intensity data for a beam passing through the middle of the plume for two conditions (a) engine off and (b) engine at full thrust. The time period shown in each case is 0.05 s, i.e., for a single ramp at 20 Hz.

The engine was in operation for approximately 50 min, and the low-frequency laser ramp was alternated between 5 and 20 Hz to compare operational performance at two different frame rates. All data were acquired as described in Section 4.

Figure 11 shows the increased variation of the raw data as the engine condition progresses from off to high-thrust condition (NH = 96.28%). The causes of the increasing signal variation can include optical effects resulting from propagation through the turbulent plume, mechanical effects due to vibration of the optomechanics and the frame, and electrical pickup from the 60 m long unshielded cables. These sources of noise have little influence on the recovered gas signals using the $2f/1f$ technique, as evidenced in Fig. 12, which shows the resulting absorption measurement for beam 14, which traverses the center of the plume. The removal of the noise apparent in Fig. 11 is due to the intensity normalization process in the $2f/1f$ technique. Of more interest are the large spikes of noise shown in Fig. 12,

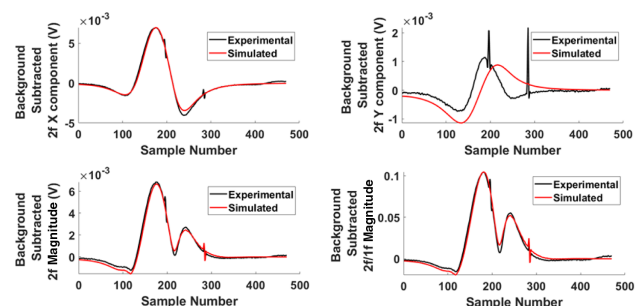


Fig. 12. $2f$ X and Y components, the magnitude of the $2f$ signal and the $2f/1f$ signal for beam number 14 when the Nd:YAG laser used for LII measurements is in operation. Also shown is the output of the model to fit concentration and temperature, showing that the LII signal has no effect on the recovered measurements.

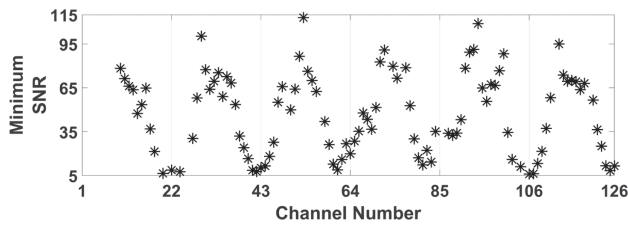


Fig. 13. SNR of all the working beams when the engine was operated at a constant thrust value of 82.65%.

which are caused by optical interference from a high-power, pulsed optical beam at 1064 nm from a Nd:YAG laser being used during the same test campaign to measure soot using the laser-induced incandescence (LII) technique. This noise appears intermittently during the test at a frequency of 10 Hz, and it is not compensated for by the 2f/1f technique, as it is being generated by another optical source. However, it is evident that it has very little effect on the fitting process, which considers the entire recovered spectrum rather than a single point in the spectrum.

To characterize the noise in the measurement data, the concentrations recovered for each beam using the 2f/1f technique, when the engine was operating at a constant thrust of 82.63%, were used. To obtain the signal-to-noise ratio (SNR) of each channel, a ratio of the mean and the standard deviation of the recovered concentration for each of the working channel was obtained for 600 frames at a constant thrust value of 82.63% as shown in Fig. 13. This measure of SNR includes all the effects of the combustion flow, mechanical vibration, ambient noise, and so on, in addition to the intrinsic noise of the measurement system. Hence, it represents a minimum value of the measurement SNR for each channel.

Figure 14 shows examples of the recovered images of CO₂ concentration using both the Landweber and Tikhonov regularization methods for the four different thrust conditions. The recovered images for both techniques are very similar both in terms of shape and maximum values for all thrust values. Using a HP laptop (HP Pavilion:15-bc202na) that has seventh-generation i7 processor with 4 cores, 16 GB RAM, and 2.8 GHz

base clock frequency, the time taken to process 2241 frames using the Landweber algorithm was about 135.11 s, whereas using the Tikhonov regularization, it took about 24.85 s to process the same number of frames. Similar to the burner test described in Section 6, the regularization parameter λ for Tikhonov regularization was determined using the L-curve method at different thrust values. At all thrust values, the corner of the L-curve was between $\lambda = 1$ and $\lambda = 50$. The Tikhonov regularization images shown in Fig. 14 have been recovered using $\lambda = 1$. For the Landweber method, the optimum value of the regularization parameter $\alpha = 0.0046$ that was obtained using the dual burner test described in Section 6 was used to recover the images for the engine test as well. Using $\alpha = 0.0046$ and the stopping criteria defined in Section 6, the number of iterations required for each frame will be different. However, for almost all the frames, the number of iterations required was less than 50. Therefore, for the Landweber method, images for all frames were reconstructed with $\alpha = 0.0046$ and 50 iterations. Figure 14 shows these recovered images at four different thrust values for the Tikhonov and Landweber methods. It can be observed from Fig. 14 that the two methods provide very similar images in terms of their shapes at different thrust values. Also, the maximum and average values of concentration in the recovered images are very similar for the two methods as shown in Figs. 15(a) and 15(b), which show their temporal evolution during the engine test period.

It is clear that the images in Fig. 14 do not show a centered, symmetric exhaust plume. It is believed the plume has been raised above the center line due to the engine lifting from its original horizontal axis during operation as observed by video and IR cameras, implying that the plume passes through the measurement ring at an upward angle with respect to the test bed floor. The distorted CO₂ distribution at the top of the images is attributed to air flow distortion caused by the engine mounting system (the “boat tail”) that mimics an under-wing mount in normal aircraft operation. In terms of their temporal resolution, we see that the concentration flux per image varies consistently with engine thrust. This is further evidenced by the temporal evolution of the maximum and average CO₂

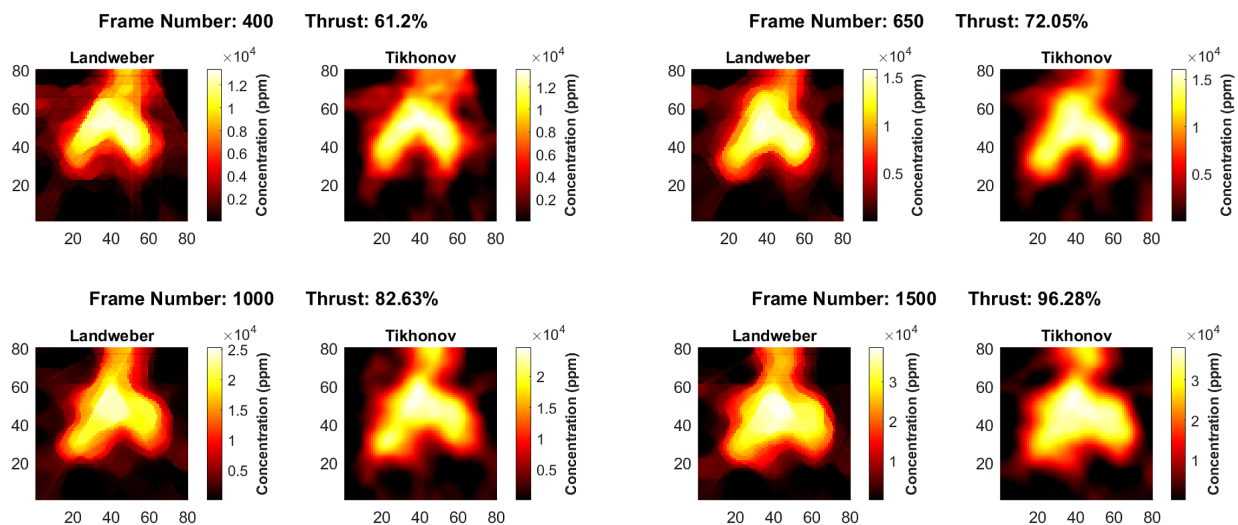


Fig. 14. Images of the temporal evolution of the CO₂ concentration for different thrust conditions. Each panel above shows the reconstructed 80 × 80 pixel image in the ROI, which is the central square of side length 165 cm in the measurement plane.

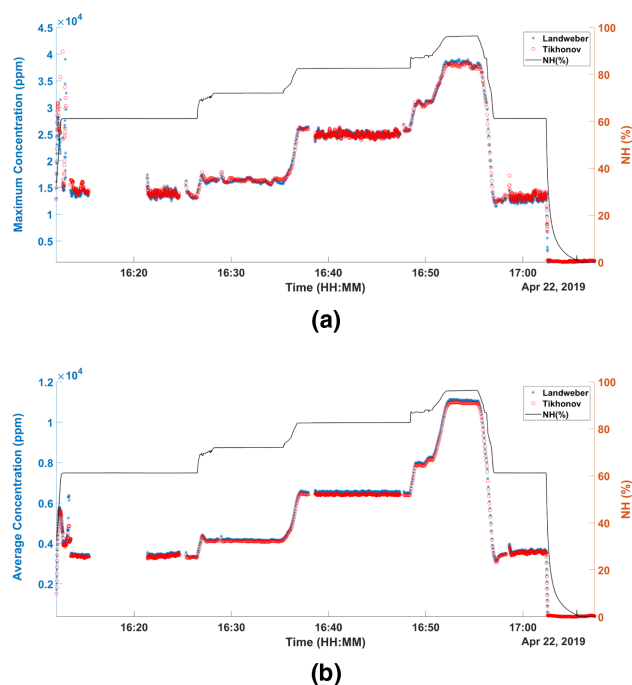


Fig. 15. Temporal evolution of (a) maximum and (b) average CO_2 concentration in each recovered frame using Landweber and Tikhonov algorithms closely follows the NH values.

concentrations of the recovered images as shown in Fig. 15(a) and 15(b), respectively, which also shows the variation in the high-pressure-compressor-shaft speed, given by the NH values, with time. Figure 15 also shows a spike in the CO_2 concentration as the NH is increased from idle ($\approx 62\%$) to 72% . This is assumed to be due to the engine operator increasing the engine thrust higher than the target and then rolling back to the desired condition. A smaller spike, assumed to be due to the same phenomenon, is apparent as the engine NH is increased from 72% to 82.5% .

As the ramp frequency was varied between 5 Hz and 20 Hz (corresponding to frame acquisition time of 3.2 s and 0.8 s, respectively), there are times when the engine was operational but imaging data was not collected. There was no significant difference between the recovered images at the two frame rates, and there was also no increased variability in the recovered path-integrated concentration measurements recovered at each frame rate.

8. DISCUSSION

The results presented in Section 2 demonstrate the care that is necessary for quantitative exploitation of near-IR absorption spectroscopy of a single target species within a complex mixture. Database spectra must be treated with great care, and it is essential to verify experimentally the key properties of the chosen absorption feature. The 2f/1f method has been found to be robust in the demanding application studied here, meeting the accuracy and low-noise requirements for CST. Ideally, the spatial distribution of temperature would be determined, as well as that of concentration. Nevertheless, the CO_2 feature used in this paper has favorable temperature dependence, providing

confidence in the concentration imaging. The multi-beam engine test data presented here were obtained from the first build of the optomechanical system design for the turbine exhaust plume environment. The system had been installed in the engine test cell for 18 months prior to these data being recorded, during which time many other in-cell operations were taking place, and many engines were tested on industry-standard cycles that typically included spells of full-thrust operation. Thus, it is considered to be a great success that robust data were recorded from more than 80% of all beams. Moreover, post-test investigations revealed a number of ways to prevent such beam losses in subsequent work. The practical implementation of the desired 100 fps DAQ system, with online 2f/1f analysis [13] has proved to be a demanding task. The NI-based system used here provided a viable alternative to perform proof-of-principle experiments, albeit at the relatively slow imaging rate of 1.25 fps and with large off-line processing load. Recent work has produced a bespoke DAQ system [47] largely based on commercially available subsystems, with bespoke signal conditioning and bespoke online processing that meets the original specifications and will be used in future CST implementations.

Several image reconstruction techniques have been applied to the data presented here, including the well-established Tikhonov regularization method and the Landweber iterative method, as discussed in Section 3, and techniques for dimensional reduction, such as the use of surrogate functions [16]. The recovered images show very similar features, although those discussed in [16] and also in [48] have the potential to provide enhanced spatial resolution in the images, as does further application-specific optimization of the Landweber method, e.g., by reducing the size of the filter window. Indeed, with six projection angles and beam separation of 75 mm, ultimate spatial resolution of ≈ 60 mm is anticipated based on [26]. The objective in this paper has been to demonstrate, as a proof of principle, the basic imaging utility of the CST system in the harsh engine test-cell environment, leaving further refinement of image reconstruction methods to be reported separately. Many different experimental phantoms were measured and reconstructed, as discussed in Section 6, enabling the image reconstruction parameters to be set. The images reconstructed from engine tests (Section 7) display a number of anticipated features: the hot exhaust plume is confined to a central region of approximately 1 m diameter; distortion is observed in the CO_2 distribution at the top of the images and is attributed to the properties of the air flow around the “boat tail”; the CO_2 plume has a ring-like structure as expected; but, unexpectedly, a substantial part of the “ring” appears to be missing at the bottom of the images. The last of these observations has been explored in great depth, e.g., by widening the reconstructed region in several stages, to check for any substantial CO_2 concentrations outside the reconstructed ROI shown in Fig. 9; none was found, despite the presence of large numbers of beam crossing points in the extension regions. While the exact cause of this feature remains to be ascertained, it appears likely to be due to the flow features associated with the closeness of the bottom of the engine to the cell floor and large items of plant placed there, and the small upward tilt of the rear of the engine and consequent upward trajectory of the plume. Further tests are desirable where the measurement plane is placed much closer to the engine exhaust

nozzle. In principle, the images of Fig. 9 could be compared with those produced in previous work that uses only two orthogonal projections [11]. However, it is simple to show that tomographic image reconstruction from such measurements alone cannot provide any spatial resolution, since the mathematical solutions would be spatially degenerate. Instead, those authors carry out a model-based optimization procedure (“simulated annealing”) that uses the measured data as a set of constraints. Hence, such a system does not facilitate tomography in the classical sense. The images presented in this paper demonstrate the critical requirement that the imaging system is able to cope with unexpected features, and hence it must depend overwhelmingly upon the inversion of the measured data. It is shown in [26] that the optimum number of (parallel-beam) projection angles is four, with reduction to three angles (with the same total number of beams) causing a very large deterioration in spatial resolution. For these reasons, no comparison is attempted between the engine data presented here and that of [11].

9. CONCLUSION

Within the harsh environment posed by the exhaust plume of a large civil aero-engine gas turbine, this paper has demonstrated that it is practicable to mount a large array of beams for simultaneous measurement of gas absorption spectroscopy. The optical system presented here comprised 126 beams arranged in six angular projections of 21 parallel beams. The optomechanical system was found to maintain good alignment for the great majority of beams for at least 18 months, during which many other in-cell operations were taking place, and many engines were tested on industry-standard cycles that typically included spells of full-thrust operation. The CO₂ absorption feature at about 1999.4 nm is found to be sufficiently understood for this work, even in the presence of combustion-produced H₂O and other exhaust species. Using the 2f/1f method of TDLs-WM spectroscopy, robust path-integrated measurements of CO₂ concentration were obtained at all thrust conditions and were observed to be resilient to various types of noise.

Tomographic imaging of the spatial distribution of CO₂ was achieved at 1.25 fps in the exhaust plume of a Rolls-Royce modern Trent engine, in a plane transverse to the plume flow. The reconstructed images were found not to be sensitive to the different types of data inversion algorithm used, the latter having been optimized using phantom tests with approximately known CO₂ distributions. The large-scale spatial features in the images are robust in spite of the loss of 25% of the total number of beams, due to various in-cell operations, which slightly degraded the spatial resolution of the images. We believe that these are the first true CST images to be obtained in a turbine exhaust plume, in that the multi-angular array permits spatial resolution of ≈ 60 mm, in principle. The tomography presented here has been focused on demonstrating the basic imaging utility of the system, and future work will ascertain the spatial resolution actually achieved. The basic properties of the reconstructed CO₂ distributions (mean value, maximum value) follow closely the power output of the engine. The gross shape of the CO₂ images confirms the expectation that the plume would occupy a region of approximately 1 m in diameter. The gross CO₂ distribution also shows a (partly) circular shape that is thought

to reflect the annular arrangement of the fuel injectors in the combustor, even at the imaging plane position, 3 m downstream from the engine exhaust nozzle. It is notable that the circle is incomplete, with a large part of its circumference ($\sim 30 - 40\%$) containing very little or no CO₂; the reasons for this remain to be confirmed by further work. The results presented here demonstrate the feasibility of imaging many different species, such as H₂O, NO_x, CO, O₂, or unburnt hydrocarbons, subject to accessing their spectroscopic features, and to associate their spatial distribution to in-combustor phenomena. The short-term prospects for greatly enhanced temporal resolution (i.e., image frame rate) are excellent. Hence, a new method of studying turbine combustion is opened up, with the potential to facilitate research and development of turbines and fuels.

Funding. Engineering and Physical Sciences Research Council (EP/J002151/1, EP/J002151/2, EP/J002178/1, EP/J00278X/1, EP/P001661/1, EP/T012595/1); H2020-EU: Combustion species Imaging Diagnostics for Aero-engine Research (CIDAR) (785539).

Acknowledgment. The authors thank Rolls-Royce for their financial support, Shell Global Solutions Ltd. for provision of aviation fuel and related advice, and Covision Ltd., DAS Photonics SL, Fianium Ltd., Gooch and Housego Ltd., Industrial Tomography Systems Plc, Innospec Environmental Ltd., M Squared Lasers Ltd., OptoSci Ltd., and Tracerco Ltd. for engineering advice, material support, and support of PhD students. The authors are also thankful to both Rolls-Royce and Instituto Nacional de Técnica Aeroespacial (INTA), Spain, for providing engineering and technical support during measurement campaigns at INTA.

Disclosures. The authors declare no conflicts of interest.

Data availability. Data underlying the results presented in this paper are not publicly available at this time but may be obtained from the authors upon reasonable request.

REFERENCES

1. I. E. Agency, “World energy outlook, 2021,” 2021. <https://iea.blob.core.windows.net/assets/4ed140c1-c3f3-4fd9-aaae-789a4e14a23c/WorldEnergyOutlook2021.pdf>.
2. I. A. T. Association, “2022-02 passenger forecast-global report,” 2022. https://store.iata.org/IEC_ProductDetails?id=9944-14&_ga=2.226972382.211006685.1651488523-1175283418.1651488523.
3. European Commission, “European aviation environmental report 2019,” 2019. https://www.easa.europa.eu/eco/sites/default/files/2021-09/219473_EASA_EAER_2019_WEB_HI-RES_190311.pdf.
4. European Commission, Directorate-General for Mobility and Transport, Directorate-General for Research, and Innovation, *Flightpath 2050: Europe’s Vision for Aviation: Maintaining Global Leadership and Serving Society’s Needs* (Publications Office, 2011).
5. H. McCann, P. Wright, K. Daun, S. J. Grauer, C. Liu, and S. Wagner, “Chapter 5 - Chemical species tomography,” in *Industrial Tomography*, 2nd ed., Woodhead Publishing Series in Electronic and Optical Materials (Woodhead Publishing, 2022).
6. W. Cai and C. F. Kaminski, “Tomographic absorption spectroscopy for the study of gas dynamics and reactive flows,” *Prog. Energy Combust. Sci.* **59**, 1–31 (2017).
7. K. Daun, “Infrared species limited data tomography through Tikhonov reconstruction,” *J. Quant. Spectrosc. Radiat. Transfer* **111**, 105–115 (2010).
8. P. Wright, N. Terzija, J. L. Davidson, S. Garcia-Castillo, C. Garcia-Stewart, S. Pegrum, S. Colbourne, P. Turner, S. D. Crossley, T. Litt, S. Murray, K. B. Ozanyan, and H. McCann, “High-speed chemical species tomography in a multi-cylinder automotive engine,” *Chem. Eng. J.* **158**, 2–10 (2010).
9. S.-A. Tsekenis, K. G. Ramaswamy, N. Tait, Y. Hardalupas, A. Taylor, and H. McCann, “Chemical species tomographic imaging of the

- vapour fuel distribution in a compression-ignition engine," *Int. J. Engine Res.* **19**, 718–731 (2018).
10. Z. Wang, Y. Deguchi, T. Kamimoto, K. Tainaka, and K. Tanno, "Pulverized coal combustion application of laser-based temperature sensing system using computed tomography-tunable diode laser absorption spectroscopy (CT-TDLAS)," *Fuel* **268**, 117370 (2020).
 11. L. Ma, X. Li, S. T. Sanders, A. W. Caswell, S. Roy, D. H. Plemmons, and J. R. Gord, "50-kHz-rate 2d imaging of temperature and H₂O concentration at the exhaust plane of a j85 engine using hyperspectral tomography," *Opt. Express* **21**, 1152–1162 (2013).
 12. S. A. Tsekenis, N. Tait, and H. McCann, "Spatially resolved and observer-free experimental quantification of spatial resolution in tomographic images," *Rev. Sci. Instrum.* **86**, 035104 (2015).
 13. E. Fisher, S. Tsekenis, Y. Yang, A. Chighine, C. Liu, N. Polydorides, P. Wright, J. Kilment, K. Ozanyan, T. Benoy, G. Humphries, D. Wilson, M. Lengden, W. Johnstone, and H. McCann, "A custom, high-channel count data acquisition system for chemical species tomography of aero-jet engine exhaust plumes," *IEEE Trans. Instrum. Meas.* **69**, 549–558 (2019).
 14. P. Wright, D. McCormick, K. Ozanyan, M. Johnson, J. Black, E. Fisher, A. Chighine, N. Polydorides, H. McCann, Y. Feng, K. Khan, P. Bastock, F. Jia, D. Hewak, J. Nilsson, M. Lengden, D. Wilson, I. Armstrong, T. Benoy, and W. Johnstone, "Progress towards non-intrusive optical measurement of gas turbine exhaust species distributions," in *IEEE Aerospace Conference Proceedings*, June 2015, pp. 549–558.
 15. P. Wright, D. McCormick, J. Kilment, K. Ozanyan, M. Johnson, J. Black, S. A. Tsekenis, E. Fisher, H. McCann, M. Lengden, D. Wilson, W. Johnstone, V. Archilla, Á. González-Núñez, Y. Feng, and J. Nilsson, "Implementation of non-intrusive jet exhaust species distribution measurements within a test facility," in *IEEE Aerospace Conference Proceedings*, June 2016, Vol. **2016**.
 16. N. Polydorides, A. Tsekenis, E. Fisher, A. Chighine, H. McCann, L. Dimiccoli, P. Wright, M. Lengden, T. Benoy, D. Wilson, G. Humphries, and W. Johnstone, "Constrained models for optical absorption tomography," *Appl. Opt.* **57**, B1–B9 (2018).
 17. T. Benoy, D. Wilson, M. Lengden, I. Armstrong, G. Stewart, and W. Johnstone, "Measurement of CO₂ concentration and temperature in an aero engine exhaust plume using wavelength modulation spectroscopy," *IEEE Sens. J.* **17**, 6409–6417 (2017).
 18. V. Ebert, K. U. Pleban, and J. Wolfrum, "In-situ oxygen-monitoring using near-infrared diode lasers and wavelength modulation spectroscopy," in *Conference on Lasers and Electro-Optics*, Technical Digest (Optical Society of America, 1998), pp. 202–206.
 19. G. B. Rieker, J. B. Jeffries, and R. K. Hanson, "Calibration-free wavelength-modulation spectroscopy for measurements of gas temperature and concentration in harsh environments," *Appl. Opt.* **48**, 5546–5560 (2009).
 20. G. Stewart, W. Johnstone, J. R. P. Bain, K. Ruxton, and K. Duffin, "Recovery of absolute gas absorption line shapes using tunable diode laser spectroscopy with wavelength modulation—part 1: Theoretical analysis," *J. Lightwave Technol.* **29**, 811–821 (2011).
 21. K. Duffin, A. J. McGettrick, W. Johnstone, G. Stewart, and D. G. Moodie, "Tunable diode-laser spectroscopy with wavelength modulation: a calibration-free approach to the recovery of absolute gas absorption line shapes," *J. Lightwave Technol.* **25**, 3114–3125 (2007).
 22. J. R. P. Bain, W. Johnstone, K. Ruxton, G. Stewart, M. Lengden, and K. Duffin, "Recovery of absolute gas absorption line shapes using tunable diode laser spectroscopy with wavelength modulation—part 2: Experimental investigation," *J. Lightwave Technol.* **29**, 987–996 (2011).
 23. K. Owen and A. Farooq, "A calibration-free ammonia breath sensor using a quantum cascade laser with WMS 2f/1f," *Appl. Phys. B* **116**, 371–383 (2014).
 24. K. Sun, L. Tao, D. J. Miller, M. A. Khan, and M. A. Zondlo, "Inline multi-harmonic calibration method for open-path atmospheric ammonia measurements," *Appl. Phys. B* **110**, 213–222 (2013).
 25. C. S. Goldenstein, I. A. Schultz, R. M. Spearrin, J. B. Jeffries, and R. K. Hanson, "Scanned-wavelength-modulation spectroscopy near 2.5 μm for H₂O and temperature in a hydrocarbon-fueled scramjet combustor," *Appl. Phys. B* **116**, 717–727 (2014).
 26. C. Liu, S. Tsekenis, N. Polydorides, and H. McCann, "Toward customized spatial resolution in TDLAS tomography," *IEEE Sens. J.* **19**, 1748–1755 (2019).
 27. M. E. Webber, M. Pushkarsky, and C. K. N. Patel, "Fiber-amplifier-enhanced photoacoustic spectroscopy with near-infrared tunable diode lasers," *Appl. Opt.* **42**, 2119–2126 (2003).
 28. S. Tsekenis, P. Nick, E. Fisher, C. Andrea, D. Wilson, G. Humphries, M. Lengden, T. Benoy, W. Johnstone, J. Kilment, P. Wright, Y. Feng, J. Nilsson, V. Archilla, J. Jia, and H. McCann, "Chemical species tomography of carbon dioxide," in *8th World Congress Industrial Process Tomography*, September 2016, Vol. **2016**.
 29. P. C. Hansen, *Discrete Inverse Problems: Insight and Algorithms* (SIAM, 2010).
 30. M. P. Wood and K. B. Ozanyan, "Concentration and temperature tomography at elevated pressures," *IEEE Sens. J.* **13**, 3060–3066 (2013).
 31. N. Terzija, J. L. Davidson, C. A. Garcia-Stewart, P. Wright, K. B. Ozanyan, S. Pegrum, T. J. Litt, and H. McCann, "Image optimization for chemical species tomography with an irregular and sparse beam array," *Meas. Sci. Technol.* **19**, 094007 (2008).
 32. L. Rothman, I. Gordon, A. Barbe, et al., "The HITRAN 2008 molecular spectroscopic database," *J. Quant. Spectrosc. Radiat. Transfer* **110**, 533–572 (2009).
 33. A. Upadhyay, M. Lengden, D. Wilson, G. S. Humphries, A. P. Crayford, D. G. Pugh, M. P. Johnson, G. Stewart, and W. Johnstone, "A new ram normalized 1f-WMS technique for the measurement of gas parameters in harsh environments and a comparison with 2f/1f," *IEEE Photon. J.* **10**, 6804611 (2018).
 34. L. Rothman, I. Gordon, R. Barber, H. Dothe, R. Gamache, A. Goldman, V. Perevalov, S. Tashkun, and J. Tennyson, "HITEMP, the high-temperature molecular spectroscopic database," *J. Quant. Spectrosc. Radiat. Transfer* **111**, 2139–2150 (2010).
 35. L. Rothman, I. Gordon, Y. Babikov, et al., "The HITRAN2012 molecular spectroscopic database," *J. Quant. Spectrosc. Radiat. Transfer* **130**, 4–50 (2013).
 36. M. Bertero and P. Boccacci, *Introduction to Inverse Problems in Imaging* (CRC Press, 1998).
 37. K. J. Daun, S. J. Grauer, and P. J. Hadwin, "Chemical species tomography of turbulent flows: Discrete ill-posed and rank deficient problems and the use of prior information," *J. Quant. Spectrosc. Radiat. Transfer* **172**, 58–74 (2016).
 38. A. Guha and I. Schoegl, "Tomographic laser absorption spectroscopy using Tikhonov regularization," *Appl. Opt.* **53**, 8095–8103 (2014).
 39. C. S. Goldenstein, C. A. Almodovar, J. B. Jeffries, R. K. Hanson, and C. M. Brophy, "High-bandwidth scanned-wavelength-modulation spectroscopy sensors for temperature and H₂O in a rotating detonation engine," *Meas. Sci. Technol.* **25**, 105104 (2014).
 40. A. Farooq, J. B. Jeffries, and R. K. Hanson, "Measurements of CO₂ concentration and temperature at high pressures using 1f-normalized wavelength modulation spectroscopy with second harmonic detection near 2.7 μm ," *Appl. Opt.* **48**, 6740–6753 (2009).
 41. J. T. C. Liu, J. B. Jeffries, and R. K. Hanson, "Wavelength modulation absorption spectroscopy with 2f detection using multiplexed diode lasers for rapid temperature measurements in gaseous flows," *Appl. Phys. B* **78**, 503–511 (2004).
 42. R. K. Hanson and P. K. Falcone, "Temperature measurement technique for high-temperature gases using a tunable diode laser," *Appl. Opt.* **17**, 2477–2480 (1978).
 43. P. C. Hansen and D. P. O'Leary, "The use of the l-curve in the regularization of discrete ill-posed problems," *SIAM J. Sci. Comput.* **14**, 1487–1503 (1993).
 44. A. Upadhyay and A. L. Chakraborty, "Calibration-free 2f WMS with in situ real-time laser characterization and 2f ram nulling," *Opt. Lett.* **40**, 4086–4089 (2015).
 45. A. Upadhyay, D. Wilson, M. Lengden, A. L. Chakraborty, G. Stewart, and W. Johnstone, "Calibration-free WMS using a CW-DFB-QCL, a VCSEL, and an edge-emitting DFB laser with in-situ real-time laser parameter characterization," *IEEE Photon. J.* **9**, 6801217 (2017).
 46. P. Hansen, *Rank-Deficient and Discrete Ill-Posed Problems: Numerical Aspects of Linear Inversion*, Vol. **MM04** of SIAM Monographs of Mathematical Modeling and Computation (SIAM, 1998).

47. G. Enemali, R. Zhang, H. McCann, and C. Liu, "Cost-effective quasi-parallel sensing instrumentation for industrial chemical species tomography," *IEEE Trans. Ind. Electron.* **69**, 2107–2116 (2022).
48. N. Polydorides, S.-A. Tsekenis, H. McCann, V.-D. A. Prat, and P. Wright, "An efficient approach for limited-data chemical species tomography and its error bounds," *Proc. R. Soc. A* **472**, 20150875 (2016).